

Mars' Background Free Oscillations

Y. Nishikawa¹ · P. Lognonné¹ · T. Kawamura¹ ·
A. Spiga² · E. Stutzmann³ · M. Schimmel⁴ ·
T. Bertrand⁵ · F. Forget² · K. Kurita⁶

Received: 18 June 2018 / Accepted: 7 January 2019
© Springer Nature B.V. 2019

Abstract Observations and inversion of the eigenfrequencies of free oscillations constitute powerful tools to investigate the internal structure of a planet. On Mars, such free oscillations can be excited by atmospheric pressure and wind stresses from the Martian atmosphere, analogous to what occurs on Earth. Over long periods and on a global scale, this phenomenon may continuously excite Mars' background free oscillations (MBFs), which constitute the so-called Martian hum. However, the source exciting MBFs is related both to the global-scale atmospheric circulation on Mars and to the variations in pressure and wind at the planetary boundary layer, for which no data are available.

To overcome this drawback, we focus herein on a global-scale source and use results of simulations based on General Circulation Models (GCMs). GCMs can predict and reproduce long-term, global-scale Martian pressure and wind variations and suggest that, contrary to what happens on Earth, daily correlations in the Martian hum might be generated by the solar-driven GCM. After recalling the excitation terms, we calculate MBFs by using GCM computations and estimate the contribution to the hum made by the global atmospheric circulation. Although we work at the lower limit of MBF signals, the results indicate that the signal is likely to be periodic, which would allow us to use more efficient stacking theories than can be applied to Earth's hum. We conclude by discussing the perspectives for the In-

The InSight Mission to Mars II
Edited by William B. Banerdt and Christopher T. Russell

✉ Y. Nishikawa
nishikawa@ipgp.fr

- ¹ Institut de Physique du Globe de Paris, Sorbonne Paris Cité, Université Paris Diderot, Paris, France
- ² Laboratoire de Météorologie Dynamique (LMD/IPSL), Sorbonne Université, Centre National de la Recherche Scientifique, École Polytechnique, École Normale Supérieure, Paris, France
- ³ Institut de Physique du Globe de Paris, CNRS-UMR 7580, University Paris 7, Paris, France
- ⁴ Institute of Earth Sciences Jaume Almera – CSIC, Barcelona, Spain
- ⁵ Ames Research Center, National Aeronautics and Space Administration (NASA), Mountain View, CA, USA
- ⁶ Earthquake Research Institute, The University of Tokyo, Tokyo, Japan

Sight SEIS instrument to detect the Martian hum. The amplitude of the MBF signal is on the order of nanogals and is therefore hidden by instrumental and thermal noise, which implies that, provided the predicted daily coherence in hum excitation is present, the InSight SEIS seismometer should be capable of detecting the Martian hum after monthly to yearly stacks.

Keywords Mars · Planetary free oscillation · GCM · Seismometer · Normal mode · InSight

1 Introduction

When a large earthquake occurs, seismic waves propagate around the entire planet for tens of hours following the event. These waves can generate standing oscillations if they fulfill the boundary conditions for specific frequencies; the standing modes are referred to as Earth's free seismic oscillations and their associated frequencies are called Earth's seismic eigenfrequencies.

The first search for Earth's free oscillations started in the late 1950 (Benioff et al. 1959) these oscillations were first observed following the great Chilean earthquake of May 1960 (Benioff et al. 1961). Further developments in long-period seismometers and global networks then allowed the normal mode frequencies to be determined, and this information was used to invert the structure models of Earth's interior, including the famous Preliminary Earth Reference Model (Dziewonski and Anderson 1981). Further inversions were done by using the splitting properties of the normal modes, which provided three-dimensional models of the Earth's structure. Woodhouse and Deuss (2015); Laske and Widmer-Schmidrig (2015); Montagner (2015) and Romanowicz and Mitchell (2015), provide an extensive description of observations of Earth's normal modes and their use in determining Earth's interior structure, while Dahlen and Tromp (1998) and Millot-Langet et al. (2002) provide a theoretical description of the same.

Thus, determining Mars' normal modes has been proposed as one of the overarching goals of a seismological mission to Mars from the early times of space exploration (Kovach and Anderson 1965; Bolt and Derr 1969) to Viking (Okal and Anderson 1978) as well as the more recent projects such as Mesur (Solomon et al. 1991), Intermarsnet (Lognonné et al. 1996) and NetLander (Lognonné and Giardini 2000). Several papers detail detection techniques have been detailed in several papers (Lognonné and Mosser 1993; Zharkov and Gudkova 1997; Gudkova and Zharkov 2004; Lognonné 2005; Lognonné and Johnson 2007, 2015). The detection of the normal modes of Mars is one of the goals of the upcoming seismic monitoring mission "InSight" which should land and deployment in 2019 and of the SEIS experiment (Tong and García 2015; Lognonné et al. 2019).

Planetary free oscillations constitute a powerful tool to investigate the internal structure of planets, as illustrated by Panning et al. (2017) with the synthetic inversion of the structure of the fundamental spheroidal normal modes. However making such long-term seismic observations on Mars obliges us to overcome several difficult problems.

One issue is related to Mars itself, which lacks plate tectonics and therefore is devoid of the large-magnitude quakes ($M > 7$) the type of which are generally used on the Earth to analyze the normal modes. All seismicity models of Mars (Phillips and Grimm 1991; Golombek et al. 1992; Knapmeyer et al. 2006) suggest that the largest quake annually is in the moment-magnitude range of 5.2–6 (i.e., 10^{17} to 10^{18} Nm). Larger quakes, although very rare, cannot be excluded.

The second difficulty is the seismic noise expected on the Martian surface, which is known to be subject to large variations in temperature and wind that generate long-period

noise much greater than anything measured in Earth's seismic vaults, where Earth's normal modes are typically observed. The InSight SEIS noise model, described in detail by Mismoun et al. (2016), suggests that, over long periods, most of the SEIS instrument noise will be related to the thermal noise, which is expected to grow below 10 mHz as $f^{-2.5}$, with amplitude at 10 mHz in the range of 1 to $2.5 \times 10^{-9} \text{ m s}^{-2} \text{ Hz}^{-1/2}$ depending on the local time. As shown by Lognonne et al. (2006), seismic signals would have larger amplitudes globally were a quake with a moment larger than $2 \times 10^{17} \text{ Nm}$ to occur on Mars. Even if such a moment corresponds to the upper limit of the annual predicted seismicity, the Poisson statistics of such a rare event suggests that several years of operation are required to attain a significant occurrence probability. Therefore, we consider herein the nonseismogenic sources of normal mode excitation.

One possible source of normal mode excitation comes from atmospheric phenomena (see Spiga et al. 2018, for a detailed review). Mars has a very active atmosphere, with weather processes generating high winds, dust devils, and storms (Read and Lewis 2004; Spiga and Forget 2009). Cloud tracking shows that Martian wind speeds easily reach 80 m/s above 30 km (Kaydash et al. 2006), whereas surface wind can be as high as 20 m/s, according to measurements by the Viking landers (e.g., Murphy et al. 1990). Measurements by the Martian landers also show that the Martian atmosphere has a regular diurnal cycle of wind and pressure (Schofield et al. 1997; Martínez et al. 2017).

The nonacoustic pressure variations associated with the global weather and the Reynolds stress associated with the wind, be it turbulent gusts in the planetary boundary layer (PBL) or high-altitude planetary-scale wind, all constitute forces to excite planetary free oscillations (Kobayashi and Nishida 1998b,a), with theoretical details in Tanimoto and Um (1999). Part of the excitation forces has frequencies within the bandwidth of the normal modes and that corresponds to the eigenfrequencies of Martian normal modes between 0.4 and 20 to 30 mHz. These particular excitation forces can globally and continuously excite the corresponding normal modes. This continuous excitation force is a possible source of Mars' background free oscillations (MBFs).

This idea for the observation of MBF was actually been suggested shortly after the first observation of Earth's background free oscillations (EBFs) (Suda et al. 1998). Oceanic excitation was initially proposed by Watada and Masters (2001). The first interpretations proposed that the entire excitation is produced by atmospheric turbulence in the Earth's PBL, which suggests that a simple scaling may exist between Earth and Mars (Kobayashi and Nishida 1998b,a). The seasonal variations in the continuous excitation later observed by Nishida et al. (2000) also support an atmospheric origin, while Tanimoto and Um (1999) proposed a simplified theory. However, the most recent studies show that the major source of continuous excitation on Earth is over the oceans (Tanimoto 2005; Rhie and Romanowicz 2004, 2006) and that, in this process, infragravity waves over the continental shelves are much more efficient seismic sources (Webb 2007) than atmospheric turbulence. However, excitation by atmospheric sources remains significantly below 5 mHz (Nishida 2013b). Note that coupled modes exist between the atmosphere and the solid earth (Lognonné et al. 1998b, 2016), and that pressure sources at the bottom of the ocean (Nishida 2014) cannot explain this larger excitation; instead, integrated atmospheric excitations at the base of Earth's atmosphere must be involved.

Observed EBFs are on the order of 0.5 nanogal ($1 \text{ nanogal} = 10^{-11} \text{ m s}^{-2}$) (Nishida 2013a) per individual mode. Stacking techniques can enhance the peak amplitude of normal modes to overcome instrument- and station-induced noise, which allows the mode eigenfrequencies to be determined. These eigenfrequencies may then be used to invert the internal structure as was done for quakes, as illustrated by Nishida et al. (2009). The same phenomenon should occur on Mars, meaning that the observation of MBFs should allow us to

determine the frequencies of fundamental spheroidal normal modes, which would constrain models for Mars' interior.

Kobayashi and Nishida (1998b) estimated the magnitude of MBFs by using a theoretical scaling based on the solar energy received by the planet (related to the planetary albedo and distance to Sun) and on the thickness of the PBL. They assumed that turbulence in the PBL provides the main excitation force for MBFs, which led them to estimate a free oscillation amplitude of several nanogals, a value quite close to that of Earth. Tanimoto (2001) estimated relative modal amplitude between Earth and Mars by using several parameters for the atmosphere and terrestrial part. Estimates of the MBF amplitude are about 30–50% of the EBFs. Lognonné (2005) and Lognonné and Johnson (2007) focused on very-long-period MBFs and, by using more realistic Martian-climate models and normal mode summations, produced MBF seismograms for periods ranging 300 to 400 s, which correspond to angular orders 12 to 15. This approach is based on the assumption that, for these very long periods and wavelengths, the major source of excitation is not Reynolds stresses or nonacoustic pressure related to the PBL, but the nonacoustic pressure related to global atmospheric circulation. They estimated the free-oscillation amplitude to be several hundredths of nanogals, which corresponds to amplitudes typically ten times smaller than those of EBFs of the same angular order.

The generation of seismic waves by atmospheric activity is not only associated with nonacoustic pressure acting on the surface, but also with the acoustic waves generated in the atmosphere and converted into seismic waves at the surface. Lognonné et al. (1998b), Watada and Kanamori (2010), and Lognonné et al. (2016) simplified this concept by demonstrating that the overall excitation in the atmosphere may be estimated based on the normal modes of the coupled solid-atmosphere system and on the atmospheric force volumetric density, which acts throughout the atmosphere and is subject to wind and nonacoustic pressure fluctuations. This approach requires integrating over the full atmospheric seismogenic volume to calculate the excitation force of the atmosphere. As shown more precisely by Lognonné et al. (1994) the latter is associated with seismic forces related to nonacoustic pressure and nonlinear Reynolds stresses in the atmosphere and can be expressed as

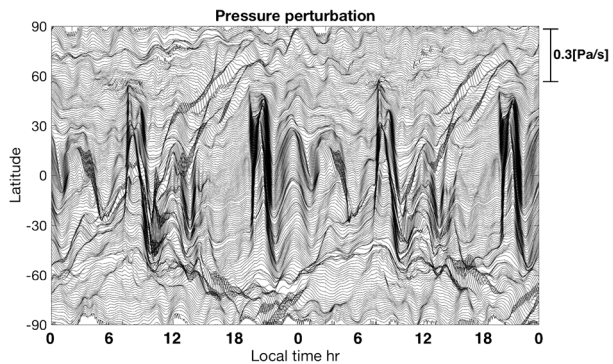
$$\Pi_i^j = -p_{glut}\delta_i^j - \rho v_i v^j, \quad (1)$$

where p_{glut} nonacoustic pressure, which is defined as $p_{glut} = p_{true} - p_{Hooke}$, where $p_{Hooke} = -\kappa \nabla \cdot \mathbf{v}$. \mathbf{v} is the atmospheric wind, ρ is atmospheric density, and p_{Hooke} is the pressure modeled by the Hooke pressure, which involves the linear model used in linear acoustics or seismology. Therefore, following the proposition made by Backus and Mulcahy (1976) for localized sources in Earth seismology and by Goldreich and Keeley (1977) for globally distributed sources in Solar seismology, we generalize here the concept of stress glut to the pressure induced by nonlinear Reynolds stresses that occur in the Martian PBL. This generalization considers that all true volumetric forces, apart from those generated by Hooke pressure, are source terms captured by the seismic moment of Eq. (1). Thus, we consider that the pressure glut and wind are respectively written as

$$p_{glut} = p_{glut,global} + p_{glut,PBL}, \quad \mathbf{v} = \mathbf{v}_{global} + \mathbf{v}_{PBL}. \quad (2)$$

Practically speaking, the wind and pressure glut associated with the PBL turbulence will be at much higher frequencies and on a smaller scale than those associated with the global circulation, but both will contribute to the overall excitation processes through Eq. (1). Therefore, the two estimates seem to provide the two end members of the general case, with

Fig. 1 Pressure fluctuations in Martian atmospheric simulated by LMD GCM for Mars meridian of longitude 0° . All pressure records are demeaned and only pressure variations are shown. Vertical axis is latitude; horizontal axis is local time [hr]. The largest pressure fluctuations occur at sunrise and sunset. The pressure fluctuations repeat to high-precision day after day. This strong daily repetition is not common on Earth



Lognonné and Johnson (2007) focusing on the global part of the excitation and Kobayashi and Nishida (1998b) focusing on the PBL part.

Major differences in PBL thickness exist between the Earth PBL, which ranges from 0.2 to 2 km and the Martian PBL, which is much thicker (about 5 to 6 km, typically) (Petrosyan et al. 2011; Spiga 2011). Because the speed of sound is less on Mars than on Earth (220 m/s compared with 340 m/s), the volumetric excitation is likely much more important on Mars than on Earth where, moreover, most of the energy of the atmospheric winds is transferred to oceanic waves, which then play a major role in the excitation of EBFs. In other words, the Earth view, where most EBF excitation may be modeled by invoking bottom-oceanic and near-surface forces, is not likely to be valid on Mars.

A first key difference is the important daily repetition of weather patterns on Mars, which is mostly related to the importance of solar flux and to the lack of a major source of other atmospheric energy, such as Earth's humidity and water. Although this initially appears in the temperature variations, which are fairly well represented by a Fourier series (see, e.g., Van Hoolst et al. 2003), it is also the case for the pressure field, as illustrated in Fig. 1, which shows the pressure variations at zero longitude as a function of local time and of latitude over two sols, as generated by a typical GCM. Such sol repetition also appears in the signal, when the latter is filtered in the frequency bandwidth of the normal modes. This is shown in Fig. 2, which corresponds to the signals of Fig. 1, but is filtered between 1 and 2 mHz (i.e., periods between 1000 and 500 s) and by Fig. 3, where the bandwidth is higher and corresponds to 2 to 3 mHz (i.e., periods between 330 and 500 s).

In this paper, we expand these past studies by using higher-resolution GCMs developed recently by the Laboratoire de Météorologie Dynamique (LMD) (see e.g., Forget and Lebonnois 2013) to better estimate normal mode amplitudes and to analyze whether the repeating atmospheric sources significantly impact the excitation of normal modes, including terms of stacking strategies. These GCMs can resolve all the large-scale Martian atmospheric processes and variabilities such as thermal tides, baroclinic waves, and planetary-scale waves (Haberle et al. 1999; Forget et al. 1999). Turbulent motions in the PBL are, by design, left unresolved in GCMs; their study requires large-eddy simulations (Spiga and Lewis 2010). This will not be included for the excitation force investigated herein [note that atmospheric excitation by small-scale turbulence in the PBL is addressed by Kenda et al. (2017) and Murdoch et al. (2017)].

Normal mode amplitudes are computed from GCM results by summing the normal modes, which estimates the signals that may be recorded by the InSight SEIS VBB seismometer (Lognonné et al. 2015; Lognonné et al. 2019). Compared with previous studies, the present study provides not only better lower estimates of MBF normal modes and ex-

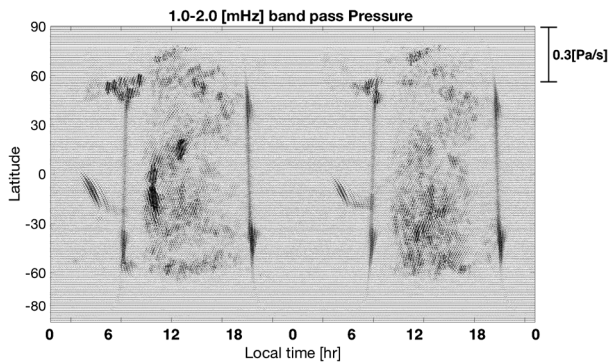


Fig. 2 Pressure fluctuations in Martian atmosphere in frequency band where normal modes concentrate in normal mode band. We applied a 1.0–2.0 mHz band-pass filter to the raw pressure data (shown in Fig. 1). The daily repetition of Martian weather processes appears clearly shown in the pattern. The band of the pattern at 1.0–2.0 mHz corresponds to low MBF frequencies (angular order 2 to 8) MBFs frequencies. The pressure fluctuations in the atmosphere excite daily coherent MBFs

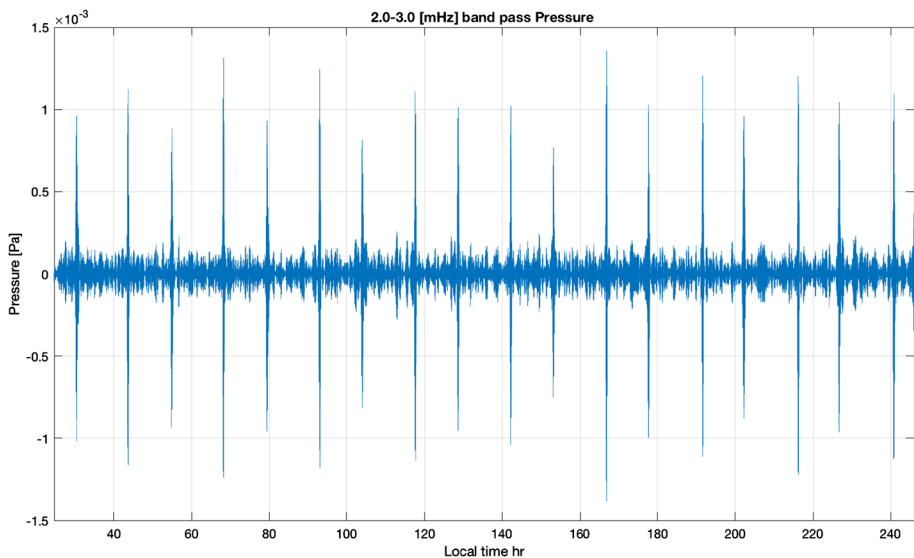


Fig. 3 Pressure fluctuations in Martian atmosphere at frequency band where normal modes concentrate at normal mode band. We applied a band-pass filter between 2.0 and 3.0 mHz to the raw pressure data (shown in Fig. 1). The large pressure fluctuations in this band occur twice a day (at sunrise and sunset). The frequency band corresponds to middle degree MBFs (angular order 9 to 15). Normal modes at this frequency are sensitive to the upper mantle (see Fig. 5)

tension to higher frequencies than Lognonné and Johnson (2007, 2015), but also pathways for the future processing of InSight measurements. Our synthetic signals will be compared with the expected noise and used to test stacking strategies, with a special emphasis on possible coherent stacking techniques made possible by the daily repetition of Martian weather. Finally, we conclude by estimating the probability of detecting MBFs with the SEIS seismometer.

2 Martian Global Climate Modeling for Normal Mode Computation

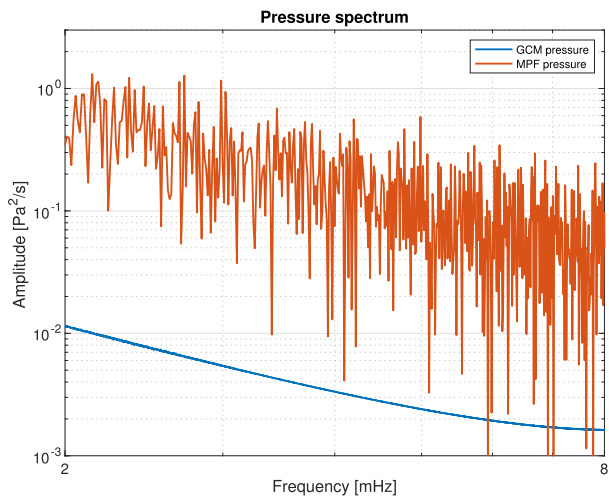
To predict the atmospheric excitation force, we used Mars Global Climate Model (GCM) which is designed to simulate large-scale atmospheric dynamics over an entire planetary sphere. The characteristics of the model are described in detail in Forget et al. (1999). We use the latest, most realistic, version of the model, which features interactive dust transport (Madeleine et al. 2011), radiatively active water and ice clouds (Navarro et al. 2014), and a thermal plume model for the boundary layer (Colaïtis et al. 2013).

Computing normal mode excitation requires a GCM simulation that is able to characterize the Martian atmospheric temporal variability of pressure and winds in the Martian atmosphere at 0.01 Hz (period 100 s), with a horizontal resolution suitable for normal modes, (i.e., 10° latitude and longitude). These requirements, dictated by seismic computations, are somewhat paradoxical from a meteorological point of view. A timescale of 100 s is associated with atmospheric circulations evolving over typical spatial scales of tens to hundreds of meters, which are challenging to resolve with GCMs, even with the best available supercomputing cluster. Most of the 100 s variability of the Martian atmosphere is instead captured through limited-area, turbulence-resolving modeling [large-eddy simulations; see, e.g., Spiga and Lewis (2010); see also Kenda et al. (2017), Murdoch et al. (2017) for a discussion of local seismic signature]. The remainder of this variability (i.e., the contribution that is not caused by microscale turbulence) is associated with mid-latitude baroclinic fronts and regional slope winds (which impact the global dynamics) and can be satisfactorily simulated through GCMs with a horizontal resolution of 1° . Conversely, nearly three decades of Mars GCM studies have consistently demonstrated that the global dynamics (at spatial scales of about 10° latitude and longitude) are well simulated by using a typical time step of 925 s in the GCM.

We also ran Martian GCM simulations specifically tailored for the seismic computations. The LMD GCM simulations used a 60 s time step, 360 longitude grid points, and 180 latitude grid points, corresponding to a mesh spacing of $1^\circ \times 1^\circ$ and a horizontal resolution of 60 km [in a setting akin to the GCM simulations described in Pottier et al. (2017)]. In the vertical direction, 25 levels are typically used with most of the levels located in the first 15 km to ensure a suitable resolution in the lower troposphere and in the boundary layer. Above 10 km, the vertical resolution is about one scale height and the altitude of the top level is about 60 km, which corresponds to about 6 scale heights. This vertical grid thus offers both the refined near-surface resolution and the accounts for the vast majority of the atmospheric mass, which allows us to deal with all possible seismic coupling in subsequent computations. It is important to note that turbulent motions developing at high frequency are not resolved by the GCM: the PBL mixing they cause is parameterized in the LMD GCM by dedicated schemes (Colaïtis et al. 2013). The GCM results used to compute normal modes thus only feature atmospheric variability at scales ranging from regional to global, and frequencies typically of the order 10^{-3} Hz (and below).

Typical GCM simulations of the Martian climate are needed so that the resulting analysis of normal modes applies to the conditions of the InSight mission. However, this does not require, however, as many simulations as would be expected from equivalent terrestrial studies. Both the low thermal inertia of the Martian surface and the fast radiative timescale of the thin Martian atmosphere imply a very low Martian-climate inter-annual variability (except during the dust storm season, but InSight will land in 2018 at the end of this season) (Read and Lewis 2004). Furthermore, given the key role played by the atmospheric-dust loading in driving the Martian climate as well as the small inter-annual variability of this parameter in the first half of the Martian year (Montabone et al. 2015) running one GCM

Fig. 4 Spectrum of GCM pressure and observed pressure. The observational data were acquired by Mars Pathfinder (LS = 170°). The GCM spectrum is computed for the same location as the observational data of Mars Pathfinder (LS = 0°). The results differ by an order of magnitude, implying that GCMs cannot fully explain the observed energy, which is likely due to inadequate modeling in GCMs of local-scale turbulences. Thus, MBFs calculated by using GCMs should be regarded as a lower limit of possible excitations



simulation for the year in which the InSight mission occurs will provide sufficiently accurate predictions for all Martian years (outside the dust storm season). The dust scenario used thus corresponds to the Martian Year 27 which is a typical clear atmosphere scenario (dust visible opacity around 0.2) with no effects from a global dust storm. GCM simulations start at $L_s = 0^\circ$ (northern spring), which corresponds to the first months of the InSight mission on Mars, and are performed for 20 Martian sols with a fixed dust profile. Given that gravity waves are partly resolved in our $1^\circ \times 1^\circ$ GCM simulation, we do not use the subgrid-scale scheme to model the effect of those waves on the large-scale flow. The outputs of the model, which are used as inputs for the modeling of the seismic moment density, as defined by relation Eq. (1), and are surface pressure and temperature, as well as atmospheric density, temperature, and winds.

The observed atmospheric status differs from that predicted by the GCM, despite the location being the same. This is illustrated in Fig. 4 for the Pathfinder location. Parts of these discrepancies are related to both the pitot pressure (associated with local wind) and to the local-scale eddies, which are not resolved by the GCM but are discussed above.

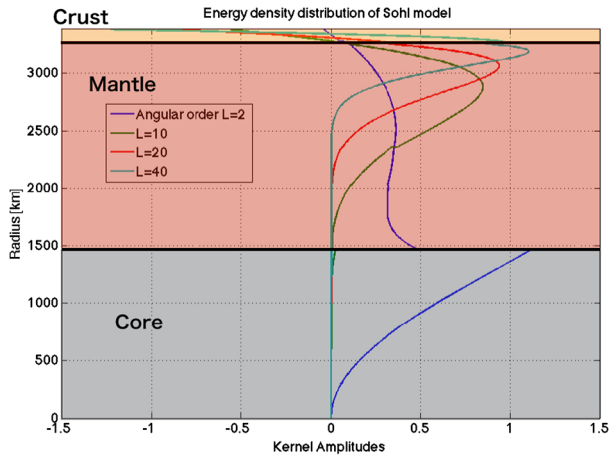
As we mentioned above, this is a challenging problem because our approach relies on GCMs. It is dependent on the environment in which the observation is made, the season, and other factors, notably, that GCMs lose energy at Martian normal mode frequencies (Fig. 4).

3 Estimating the Amplitude of Martian Normal Modes

3.1 Internal Structure Model

Martian internal models have been discussed by many researchers; please see Panning et al. (2017) and Smrekar et al. (2018) for further descriptions and review. The biggest differences between these models are in the crustal thickness and core radius. The first estimates are based on observation and laboratory experiments. A large amount of information about the inner structure is based on gravitational observations and data on surface-soil properties. With the constraints of mean density, moment of inertia, and k_2 Love number, the inferred radius of the core is estimated to be 1600 ± 200 km (Khan and Connolly 2007; Sohl and

Fig. 5 Vertical amplitude of spheroidal fundamental normal modes in solid part. Low-degree normal modes are low frequency. Large-amplitude areas concentrate the models energy and sensitivity. Low-degree waves (angular order 2 to 9) are sensitive at the core and deep mantle. High-degree waves (angular order 10 to 39) are sensitive at the middle and shallow part of the mantle. Each mode is sensitive at a different depth



Spohn 1997; Spohn et al. 2001; Rivoldini et al. 2011). However, only normal modes with very long periods are sensitive to the core size and, furthermore, their amplitude near the surface depends only weakly on core size. Consequently, the choice of internal model is not critical for our estimate of MBF amplitude, and all models will provide similar results. In the present work, we use the Sohl model to generate a reference internal structure. We calculate fundamental spheroidal normal modes longer than 120 s, and the limitation of the period is dictated by the GCM time step. This corresponds to calculating spheroidal normal modes of angular orders between $\ell = 2$ and $\ell = 39$ and of radial order $n = 0$ which constrains the core and the deep, middle mantle (Fig. 5).

3.2 Normal Modes Excitation

The theory of normal mode excitation and of normal mode summation is described in several papers (see, e.g., Lognonné 1991; Dahlen and Tromp 1998; Lognonné 2002) so we only briefly summarize the approach here. Martian global oscillations are governed by the gravito-elastic equation (when attenuation is neglected) or by the gravito-anelastic equation, when anelastic processes are considered. Atmospheric normal modes may also be computed by using the theory developed by Lognonné et al. (1998a). Lognonné et al. (2016) studied attenuation processes in the Mars atmosphere due to both the viscosity and CO₂ molecular relaxation. They concluded that, for long periods (e.g., $T \geq 50$ s), no significant atmospheric attenuation should be expected in the lower atmosphere where the greatest excitation force is concentrated, suggesting that an adiabatic approximation of the atmosphere suffices for our modeling. The starting equation is

$$-\omega_k^2 \rho_0 \mathbf{u}_k + \mathbf{A}(\mathbf{u}_k) = \mathbf{f}, \tag{3}$$

where ω_k is the angular eigenfrequency, \mathbf{u}_k is the associated displacement eigenfunction, \mathbf{A} is the gravito-elastic operator (or gravito-anelasto operator), ρ_0 is the unperturbed density and \mathbf{f} is the external force. The gravito-elastic operator \mathbf{A} is defined for the internal structure model and is given by:

$$\mathbf{A}(\mathbf{u}) = \nabla(\delta \mathbf{T}_{elastic} - \mathbf{u} \cdot \nabla \mathbf{T}_0) - \mathbf{g} \nabla \cdot (\rho_0 \mathbf{u}) + \rho_0 \nabla \Phi, \tag{4}$$

for the solid part, where Φ is the mass-redistribution potential, \mathbf{g} is the gravity acceleration due to gravity, \mathbf{T}_0 is the pre-stress and $\delta\mathbf{T}_{elastic}$ is the elastic stresses. The operator in the atmospheric part can be written by using $\mathbf{T}_0 = -p_0\mathbf{I}$ and

$$\mathbf{T}_{elastic} = -p_{Hooke}\mathbf{I} = \kappa\nabla \cdot \mathbf{v}\mathbf{I}, \tag{5}$$

where \mathbf{I} is the identity tensor. The result is

$$\mathbf{A}(\mathbf{u}) = \nabla(\kappa\nabla \cdot \mathbf{u} + \mathbf{u} \cdot \nabla p_0) - \mathbf{g}\nabla \cdot (\rho_0\mathbf{u}) + \rho_0\nabla\Phi, \tag{6}$$

where κ is the bulk modulus and p_0 is the equilibrium pressure. Following Lognonné et al. (1994), we can write the momentum-density field $\rho\mathbf{v}$ in the form

$$\rho(\mathbf{r}, t)\mathbf{v}(\mathbf{r}, t) = \rho_0(\mathbf{r}) \sum_k \dot{c}_k(t)\mathbf{u}_k(\mathbf{r}), \tag{7}$$

which provides the displacement field \mathbf{u} , which can be expressed to first order (and therefore sufficiently far enough from the sources when on location) as

$$\mathbf{u} = \sum_k c_k(t)\mathbf{u}_k(\mathbf{r}). \tag{8}$$

We get the differential equation with respect to time and the source function as

$$\frac{\partial^2 c_k(t)}{\partial t^2} + \omega_k^2 c_k(t) = \Psi_k(t), \tag{9}$$

where Ψ_k is the excitation force for each mode. To compute the normal mode excitation forces, we consider the nonlinear equation of momentum conservation,

$$\begin{aligned} \frac{\partial}{\partial t}(\rho\mathbf{v}) &= -\nabla p + \rho\mathbf{g} - \nabla \cdot (\rho\mathbf{v}\mathbf{v}), \\ &= -\nabla p_{Hooke} - \nabla \cdot (\rho\mathbf{u})\mathbf{g} - \nabla\delta p_{glut} - \nabla \cdot (\rho\mathbf{v}\mathbf{v}), \\ &= -\mathbf{A}(\mathbf{u}) - \nabla\delta p_{glut} - \nabla \cdot (\rho\mathbf{v}\mathbf{v}), \\ \delta p_{glut} &= p - p_0 + \kappa\nabla \cdot \mathbf{u} + \mathbf{u} \cdot \nabla p_0, \\ \delta p_{Hooke} &= -\kappa\nabla \cdot \mathbf{u} - \mathbf{u} \cdot \nabla p_0, \end{aligned} \tag{10}$$

where p_0 is the equilibrium pressure and $p_{glut} = p_0 + \delta p_{glut}$ is the GCM pressure as the GCM filter acoustic waves. We assume here that the gravity term is linear and therefore excluded from this term excitation processes associated with nonlinearity (Julián et al. 1998). If existing in the Martian atmosphere, (e.g., for atmospheric gravity waves), this might be therefore an additional excitation term for frequencies below the 2 mHz acoustic cutoff (Lognonné et al. 2016). However, transport terms are fully included in the Reynolds stress term $\rho\mathbf{v}\mathbf{v}$.

Note also that the GCM pressure variations are much greater than those generated by the flow, so that $\delta p_{glut} \approx p - p_0$. We project Eq. (10) onto a given normal mode, which gives

$$\begin{aligned} \int_V dV \mathbf{u}_k \cdot \frac{\partial}{\partial t}(\rho\mathbf{v}) &= \ddot{c}_k, \\ &= - \int_V dV \mathbf{u}_k \cdot \mathbf{A}(\mathbf{u}) - \int_V dV \mathbf{u}_k \cdot [\nabla\delta p_{glut} + \nabla \cdot (\rho\mathbf{v}\mathbf{v})], \end{aligned}$$

$$\int_V dV \mathbf{u}_k \cdot \frac{\partial}{\partial t}(\rho \mathbf{v}) = \ddot{c}_k, \tag{11}$$

$$= -\omega_k^2 c_k(t) - \int_V dV \mathbf{u}_k \cdot [\nabla \delta p_{glut} + \nabla \cdot (\rho \mathbf{v} \mathbf{v})].$$

Note that, in this projection, we shall decompose the volumetric integration for all partial volumes (in practical terms, the atmosphere and interior) i separated by discontinuities j , such that

$$\int_V dV \mathbf{u}_k \cdot [\nabla \delta p_{glut} + \nabla \cdot (\rho \mathbf{v} \mathbf{v})]$$

$$= \sum_i \left[\int_{S_i} dS [\delta p_{glut} \mathbf{u}_k \cdot \mathbf{n}_i + \rho \mathbf{u}_k \cdot \mathbf{v} \mathbf{v} \cdot \mathbf{n}_i] - \int_{V_i} dV \nabla \mathbf{u}_k \cdot \mathbf{m} \right]$$

$$= - \int_V dV \nabla \mathbf{u}_k \cdot \mathbf{m} + \sum_j \int_{S_j} dS [\mathbf{u}_k \cdot \mathbf{n}_j \delta p_{glut}]_{\pm} \tag{12}$$

where we assume no vertical winds at the interface. (Note that this approach is here limited to a spherical surface and that additional excitation terms could occur due to topography, in way similar to what occurs for Earth's hum [see, e.g., Nishida (2017)]. The vector \mathbf{n}_i is the normal to the surface, leaving the volume i , denoted $+$ and $-$ the volume against $+$, for which the normal vector is oriented in the opposite directions. Following Lognonné and Mosser (1993), we define here the flux-glut moment density tensor as

$$m^{ij} = (p + \kappa \nabla \cdot \mathbf{u}) \delta^{ij} + \rho v^i v^j. \tag{13}$$

Equation (12) simplifies further because we have not only continuity of pressure at the atmosphere-solid interface, but also continuity of the Hooke pressure and the vertical amplitude of modes across this interface. We therefore identify the second term as the excitation coefficient, which can be rewritten as

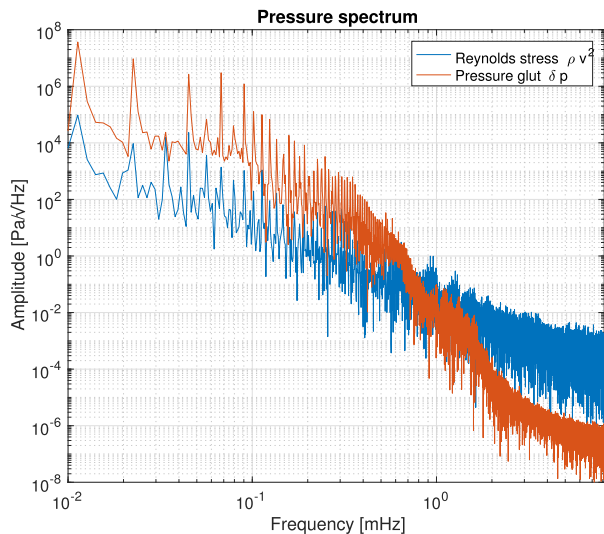
$$\Psi_k(t) = - \int_V dV \mathbf{u}_k \cdot \nabla [\delta p_{glut} + \cdot (\rho \mathbf{v} \mathbf{v})] = \int_V dV \epsilon_k : \mathbf{m}, \tag{14}$$

where ϵ_k is the strain tensor of the normal mode k . Figure 6 shows the pressure and Reynolds stress spectra for an arbitrary point on the surface of Mars, as calculated by the GCM. Note that the amplitudes decrease as $1/f$. Most of the variability in the normal mode bandwidth is associated with the Reynolds stress. All terms in Eq. (13) can be derived from the values calculated by the GCM, thereby giving us a full description of the moment tensor based on the GCM results.

3.3 Normal Modes Amplitudes in Atmosphere

Estimating the normal modes excitation coefficients $\Psi_k(t)$ requires knowledge of the normal mode amplitude in the atmosphere. Given the exponential decay of the density and the a priori thickness of the Martian boundary layer, most of the pressure glut release will occur in the first 10 km so we focus on computing the normal modes at these relatively low altitudes. Normal mode atmospheric amplitudes are affected by many factors, such as viscosity, radiative boundary, sound velocity, relaxation, resonance, etc. See Lognonné et al. (2016) for more details on the different parameters affecting the amplitude modeling. At low altitudes

Fig. 6 GCM pressure and Reynolds stress power spectrum. The pressure glut is stronger (weaker) than the Reynolds stress at low (high) frequencies. At high frequencies, the main contribution to the pressure variation is eddies, which generate Reynolds stress through wind variations



and in the bandwidth of normal modes, viscous and relaxation processes can be neglected, as done by Lognonné and Johnson (2007). However both Lognonné and Johnson (2007, 2015) and Lognonné et al. (2016) assume the atmosphere to be spherically, symmetric and rigorous. The three-dimensional computation of the normal modes requires a prohibitive amount of computing time. Although the interior structure of Mars can be considered spherically symmetric, the acoustic properties of the Martian atmosphere depend strongly on local time, with large variations between the night and day for the height scale, temperature, and density, and therefore for the sound speed and acoustic impedance as well as the coupling between ground and atmosphere. This is illustrated in Fig. 7, which shows the variation of atmospheric scale height. Relative variations of $\pm 20\%$ with LS (or during one day at the same longitude) are observed, which suggest that lateral variation of the atmospheric coupling should be accounted for in MBF calculations. Furthermore, Mars has larger lateral atmospheric variations than does Earth. The main driver of atmospheric variation is temperature: on Mars, temperature variations are much greater than on Earth because of the absence of oceans and atmospheric water vapor, which serve as effective thermal reservoirs and stabilize the temperature. Thus, the MBF with three-dimensional atmospheric structure must be estimated to better understand the signal levels of MBFs and perfect the simulations. However, to account for the lateral variation while maintaining a realistic calculation time requires some modeling and simplification. Thus we simplified the atmospheric structure by neglecting viscosity, radiative boundaries, relaxation, and resonance.

In this paper, we propose to compute the amplitude of the atmospheric normal modes by propagating the normal mode amplitude at the surface into the atmosphere. In other words, instead of directly calculating normal modes in the atmosphere, we extrapolate the modes calculated for the solid part of the planet into the atmosphere. For this purpose, we make the following assumptions:

- the normal mode phase velocity is much greater than acoustic-wave velocity, leading to a vertically longitudinal upward-moving acoustic wave;
- the normal modes interact asymptotically with the atmosphere and without significant resonance between solid and atmosphere, which limits this approach to normal modes above the atmospheric cutoff frequency.

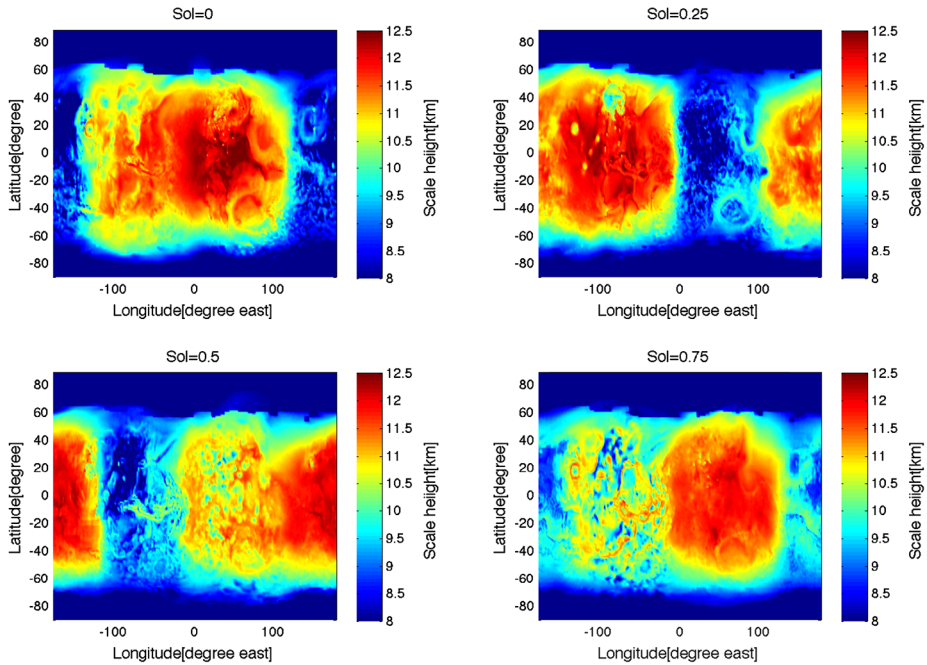


Fig. 7 Daily variation of atmospheric scale height. The red (blue) areas are thick (thin). Because of the large temperature variations, the scale height thickness changes from 8 to 12 km in one day. During the day, the atmosphere expands to 12 km height, whereas it shrinks to 8 km height at night. This variation in scale height directly affects the normal mode structure, and the isosphere model cannot describe this lateral effect

Given these two assumptions, the wave-propagation normal mode is

$$u_k(z) = u_k(0) \cdot e^{-ik_z z} \times \sqrt{\frac{\rho(0)c(0)}{\rho(z)c(z)}}, \tag{15}$$

where k_z is a vertical wave number and z is the altitude above the ground. The first factor on the right side of the equation is the wave-propagation factor and the second factor is the wave transmission ratio. With the wave-propagation method, we can describe the local time and, more generally, how the normal mode amplitude in the atmosphere depends on geography.

We compare the resulting amplitudes with those computed by using the more precise model of Lognonné et al. (2016). For angular orders $\ell \geq 10$, the difference is less than the effect of the lateral variation (see Fig. 8). However, for smaller angular orders and for modes with frequencies close to or below the atmospheric cutoff, this simple propagation fails and large discrepancies appear because of acoustic-wave reflection and resonance in the atmosphere. Figure 10 shows the relative atmospheric energy for the fundamental spheroidal modes. The energy peaks around 2.2 mHz, which corresponds to the angular order $\ell = 9$. This large coupling of the normal mode with angular order $\ell = 9$ is normal if also seen on the mode amplitude (Fig. 9).

Such modes, thus require exact computation. Note, however, that these modes are also difficult to observe because of the expected high very low-frequency modes associated with temperature fluctuation below 5 mHz.

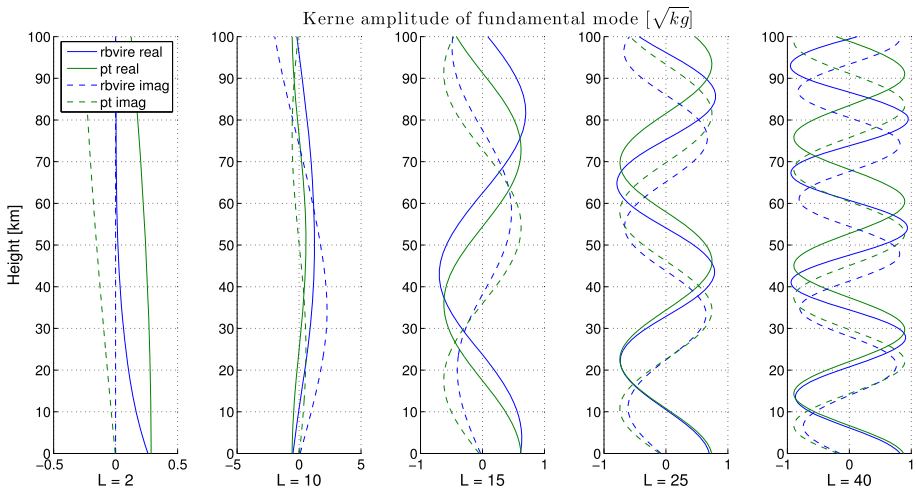


Fig. 8 Kernel sensitivity of normal modes in air. Blue curves include the radiative boundary, viscosity, and relaxation. Green curves include only wave propagation and transmission. Solid lines and dotted lines show the real part and imaginary parts, respectively. For order $n \Rightarrow 10$, the gaps between two adjacent normal modes are much less than the scale height

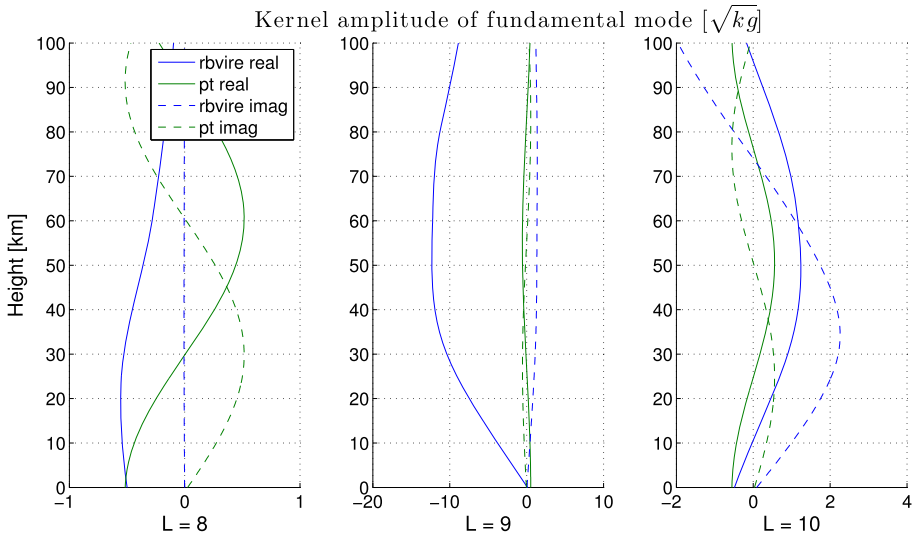


Fig. 9 Kernel sensitivity of normal modes in air. At the normal mode of angular order nine, the large gaps occur because of the resonance between the atmosphere and the solid part. The normal mode cannot describe this resonance, so the normal mode calculation only works for angular order 10. Below angular order 10, normal modes are hard to detect because of the low-frequency thermal noise (see Sect. 4.2)

Fig. 10 Relative atmospheric energy of surface wave in the Mars atmosphere for Rayleigh surface waves as a function of frequency. Associated angular order values range from $\ell = 2$ to $\ell = 39$. The peak of the fraction is at angular order 9 (near 2.2 mHz). At the first peak, a strong resonance appears between the atmosphere and the solid part

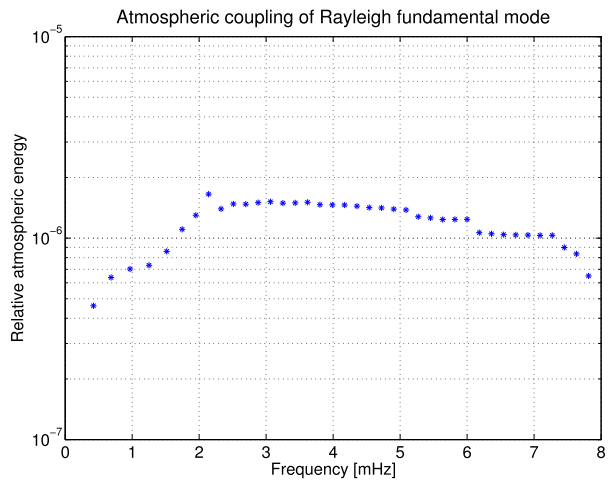
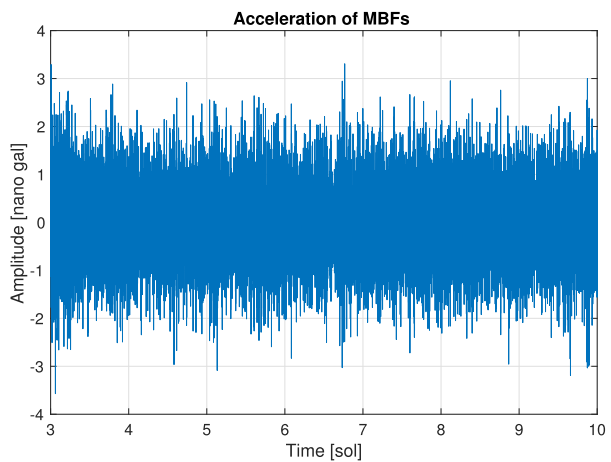


Fig. 11 7 MBF acceleration as a function of Martian days. The MBF is the sum of fundamental normal modes of angular order 2 to 39. The amplitude is given in nanogals (10^{-11} m/s^2). The MBF continues for days because the normal modes are excited by continuous atmospheric activities. The data for the first three sols are meaningless due to the GCM boundary conditions and the stability of MBFs

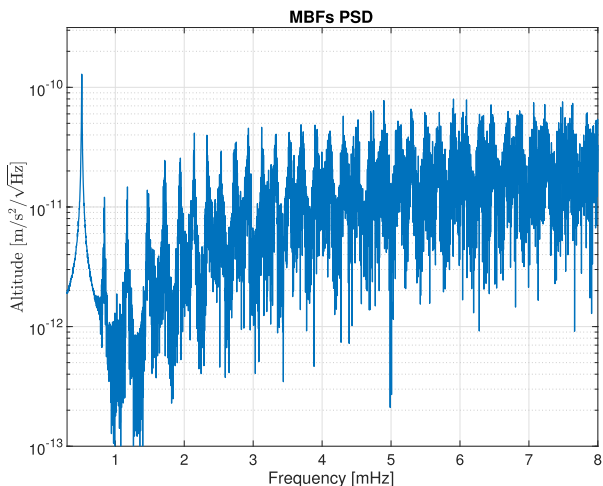


4 Results and Discussion

4.1 Normal Modes Amplitude

The MBF is obtained by summing the fundamental Rayleigh normal modes, with the amplitude of each computed by using Eqs. (8) and (11). For this study, we summed the fundamental normal mode for degrees $\ell = 2$ to $\ell = 39$. The amplitude of the MBF signal is a few nanogals (10^{-11} m/s^2), as shown in Fig. 11. This amplitude is greater than that reported by Lognonné and Johnson (2007, 2015), which is likely because of the larger angular orders and therefore larger frequencies that they used. Since the signal is the sum of all normal modes, specific peak amplitudes are more clearly shown in Fig. 12. The lowest-frequency peak (0.4 mHz) is a normal mode of angular order 2, whereas the highest-frequency peak (8.3 mHz) is a normal mode of angular order 39. Note, however, that the amplitudes are well modeled only for frequencies greater than 2 mHz. We also observe a gradual increase of the amplitude with frequency up to 5 mHz, after which the amplitude of the peaks remains constant.

Fig. 12 Calculated spectrum of acceleration power density of MBFs. The MBFs are estimated by using GCMs and the internal structure given by the Sohl model. The normal mode frequencies come from power spectral density calculations. Each peak is a normal mode; there are 38 peaks in this figure, ranging from angular order 2 to 39. The amplitude grows with frequency up to 5 mHz and is then remains constant for frequencies ≥ 5 mHz



4.2 Normal Modes: Detection and Seismometer Performance

MBF amplitudes are quite small and so can be detected only by using instruments with high sensitivity and low noise. Let us consider whether these modes can be detected in the POS output of the InSight SEIS VBB sensors. This output has a flat acceleration gain in the frequency bandwidth of normal modes (see Lognonné et al. 2019).

The least significant bit (LSB) of the InSight SEIS seismometer for differential output is

$$LSB = \frac{2 \times Voltage}{Gain}. \tag{16}$$

The seismometer voltage is ± 25 V, the acquisition dynamics is 24 bit, and the gain is $\approx 10^4$ V/DU for low gain mode and about 4.5 times greater for high gain mode. Therefore, the LSBs are

$$LSB_{LG} = \frac{2 \times 25}{10^4 \times 2^{24}} = 30 \text{ nanogal}, \tag{17}$$

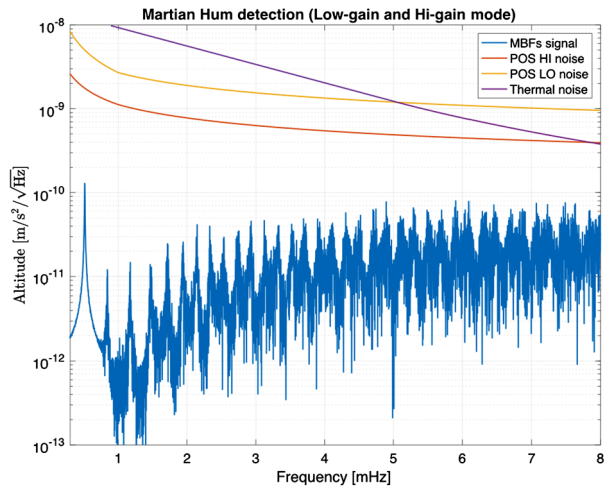
$$LSB_{HG} = \frac{2 \times 25}{4.5 \times 10^4 \times 2^{24}} = 6.6 \text{ nanogal}.$$

The amplitude of MBFs is only nanogals and the LSBs are therefore greater. The real ground acceleration signal contains MBF, as well as thermal drift, thermal and instrument noise, and possibly seismic signal. For a more realistic evaluation, we approximate the daily temperature variation associated with the temperature sensitivity of the sensors with an ideal sinusoidal curve and superpose it on the MBFs. Because this drift is much greater than 1 LSB, it enhances the MBFs up to a detectable level. The sinusoidal thermal-noise model is given by

$$A_{temp}(t) = \gamma \delta T \left(1 - \cos \frac{2\pi t}{D_{sol}} \right), \tag{18}$$

where A_{temp} is the equivalent acceleration of temperature variations, t is local time, D_{sol} is the duration of a Martian day, γ is the sensitivity per degree of the VBB in the acceleration

Fig. 13 Spectrum of power acceleration density of MBF, instrumental noise, and environmental noise. Above 5 mHz (angular order 22), thermal noise is much greater than the MBF signal. Below 6.5 mHz (angular order 30), the MBF signal overcomes both instrumental and thermal noise. During nighttime, the InSight SEIS seismometer in high-gain mode may detect the MBF signal. The MBF signals detected carry information about the middle, shallow part of the Martian mantle



unit, and δT is the temperature variation over one Martian day. The temperature sensitivity γ is set to 10^{-5} m/s²/K and daily temperature variation δT is 4 K, which corresponds to the variations expected during winter (Mimoun et al. 2016; Lognonné et al. 2019). The amplitude of this thermal daily variation is therefore 4.0×10^6 nanogal, which is six orders of magnitude greater than MBF signals.

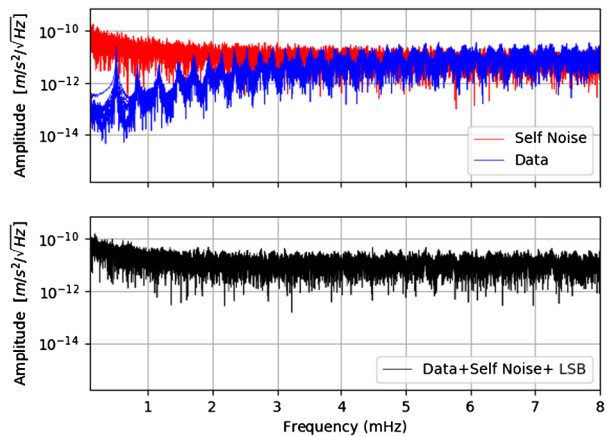
We simulate the signals by adding the MBF signal to the thermal drift, and then simulate the digitization by converting this acceleration signal into bits. Subtracting from the signal a sol-periodic sine wave with amplitudes computed by using the least-squares method simulates data processing. For both low gain and high gain, clear MBFs signal are retrieved from the residual, which demonstrates the capability of the acquisition system to use stochastic amplification of the noise to detect signals smaller than the LSB.

The signal remains much smaller than the expected instrument noise, which is the superposition of the instrument self-noise and of the residual of both the subtracted temperature drift and the potential pressure decorrelation (Murdoch et al. 2017). This is illustrated in Fig. 13, which compares the MBF spectrum to the instrument self-noise in both low gain and high gain and to the expected thermal-drift signal. In the 5 to 10 mHz band, which contains a large part of the target bandwidth for the Martian hum search (5 to 20 mHz) and the bandwidth in which our modeling hypothesis and the GCMs have acceptable errors, the MBF signal is expected to be 5 to 10 below the instrument self-noise, depending on the gain. Stacking this signal over the mission duration will then allow successful detection.

The amplitude of ideal thermal noise model is 4.0×10^6 nanogal. The acceleration is 0.4×10^6 DU in low-gain mode or 1.4×10^6 DU in high gain mode. The thermal noise acceleration is far greater than the MBF signal. Thus, no signal is detected by the InSight SEIS seismometer in low-gain mode. In high-gain mode, we can detect 1 DU signal several times per half Martian day. However, ideal thermal noise can kick up to 1 DU after the decimal point. After subtracting the digitized thermal noise, more MBF signals are detected using the InSight SEIS seismometer in both low- and high-gain mode. Although the MBF signal is hidden by the large thermal noise, after subtracting the digitized thermal noise, we capture a greater part of the MBF signal.

To improve the signal to noise ratio and detect the MBF normal modes, we further process data as follows. First, we create a trace that contains MBF signal and noise. As explained previously, noise can be decomposed as self-noise, thermal noise and LSB noise. We com-

Fig. 14 Spectrum amplitude of each two sol long segment for MBF traces (blue) and self-noise traces (red) in the top figure and for S4 traces (black) in the bottom figure



pute self-noise as the inverse Fourier transform of a spectrum whose amplitude follows the station sensitivity as a function of frequency and whose phase is random. This self-noise is added to the MBF seismogram to create a trace S1. Thermal noise is then computed as a sinus function over one sol with an amplitude of 10^{-4} m/s² to simulate the seismic acceleration generated by thermal drift. This thermal noise is added to trace S1 to create trace S2. LSB noise takes into account the least significant bit ($5.81/4 \times 10^{-11}$ m/s²). Trace S2 is modified so that the only signal above the LSB is kept and this trace is called S3. Finally, we assume that the thermal drift is known and it is subtracted to trace S3 to generate to the final trace S4.

The seismogram S4 is then cut into segments of two sols with one sol overlap, starting at sol 4. Figure 14 (top) displays spectra amplitude of each two sol-long segments for the MBF signal (blue lines) and self-noise (red lines) and confirms that the amplitude of the MBF normal modes is below the self-noise. Figure 14 (bottom) shows the spectra amplitude of each segments of trace S4 (black lines). Normal modes are not visible in the amplitude spectra of the different data segments.

Data are then processed as follows. Phase auto-correlation is computed for each segment and then stacked using the phase weighted stack method following the method developed in Schimmel et al. (2011), Ventosa et al. (2017), Schimmel et al. (2018). For comparison, we apply the same processing to MBF traces, S1 traces (MBF+self noise) and S4 traces (MBF+self noise+LSB). Figure 15 (top) show the amplitude spectra of each stack. Normal mode peaks are clearly visible for the MBF stack amplitude spectrum between 1.5 and 8 mHz. Some modes can also be detected for the stack of traces S4 at frequencies higher than 4 mHz.

In order to enhance the signal to noise ratio, we further select the Rayleigh wave train windows on the stack of auto-correlograms by setting to 0 the rest of the signal as in Deen et al. (2017). We keep signal around 0-time lag and around each surface wave train R1 to R3. We keep 6 minutes around 0 lag time and select R1 to R3 wave trains considering that their group velocities are between 3.8 and 5.7 km/s. Figure 15 (bottom) displays the new amplitude spectra, and we observe that the normal mode peaks are now clearly visible for frequencies above 2.5 mHz for the MBF stack and also for data with realistic noise (self-noise or MBF+self noise). Adding longer time series will improve the signal to noise ratio and therefore we expect that normal modes excited by the Mars atmosphere should be detectable.

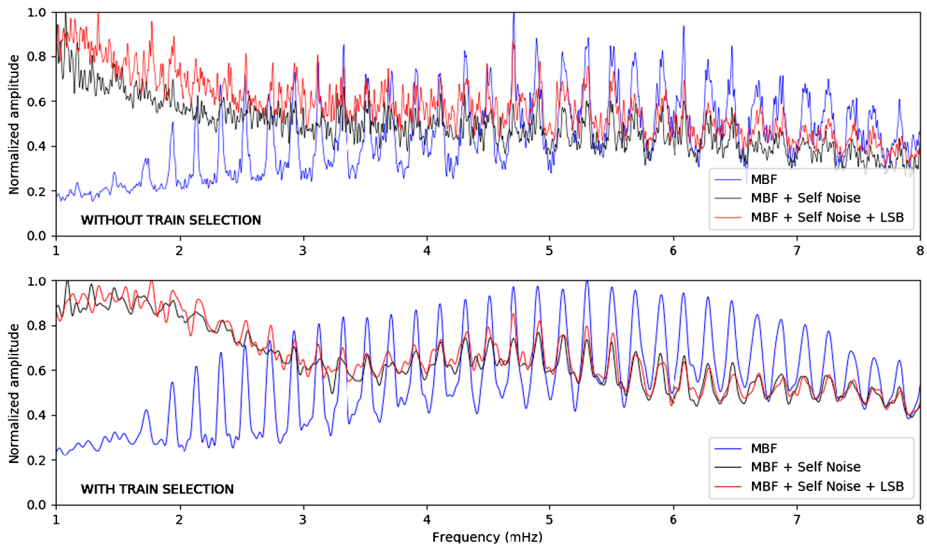


Fig. 15 Normalized spectrum amplitude of the stack of autocorrelograms without surface wave train selection (top) and after surface wave train selection (bottom). The blue, black and red curves correspond to MBF, MBF+self noise and MBF+self noise + LBS noise (S4) data respectively

4.3 Estimate of Seismic Magnitude of MBF Signal

We now not only estimate the MBF amplitude in terms of seismic magnitude, but also check that our estimate of the MBFs is comparable to that obtained by applying a simple energetic budget, following the approach of Kobayashi and Nishida (1998b).

For a first estimate, we assume that the release of acoustic and seismic energy into atmospheric activities is driven by solar flux and, furthermore, that all the energy of planetary background free oscillations comes from solar flux. This maximum energy may be expressed as

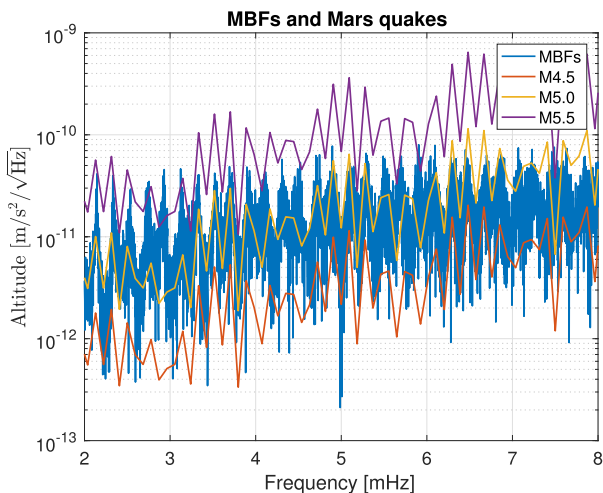
$$W_M = F_E \times \left(\frac{D_E}{D_M}\right)^2 \times (1 - A_M) \times \pi R_M^2, \tag{19}$$

where W_M is the rate at which the Sun transfers energy to the Mars surface, F is the solar flux above Earth's atmosphere ($F_E = 1360 \text{ W/m}^2$), D is the distance from the Sun ($D_M = 1.52D_E$), A is the bound albedo ($A_M = 0.25$), subscripts E and M refer to Earth and Mars, respectively, and R_M is the radius of Mars. This solar energy is converted to seismic energy, with a coherency duration of $T\sqrt{Q}$, where Q is the quality coefficient of the mode and T is its period. Thus the MBF's energy (E_{MBF}) is

$$E_{MBF} = W_M \times s \times \sqrt{Q} \times T \times C, \tag{20}$$

where $s = 0.01$ is an acoustic efficiency (which can be achieved for high-altitude winds of 40 to 50 m/s, assuming an efficiency depending on M^3 , where M is Mach number, [see, e.g., Goldreich and Kumar (1988)]). The constant C is the energy coupling ratio between the atmosphere and the solid part of Mars (a typical value is $C = 5 \times 10^{-6}$, (see, e.g., Lognonné and Johnson 2015)), Q is seismic attenuation of MBF's (typical value $Q = 100$), T is period

Fig. 16 Spectrum power acceleration density of MBF and free oscillations. The Martian atmosphere excites the MBFs and the free oscillations are excited by imaginary seismic events. The magnitude of the events are M4.5, 5.0, and 5.5. MBFs are close to M5.0 oscillations. This result is consistent with rough estimates



of MBFs (typical value $T = 200$ s). We then use the energy-magnitude relation of (Gutenberg and Richter 1956):

$$\log E = 4.8 + 1.5M, \tag{21}$$

where M is the magnitude of the seismic event. A rough estimation of the MBF magnitude gives $M = 4.9$.

We now compare the amplitude obtained by our GCM modeling with that excited by seismic activity. This is achieved by comparing the spectrum of the MBFs with those of quakes that occur at an epicentral distance of 90° . We find amplitudes of MBFs close to those generated by a M5.0 free oscillation (Fig. 16), while the estimates based on the GCM calculation are consistent with those based on solar flux. The results are also consistent with those estimated from Earth’s hum, which has been estimated to be equivalent to a daily earthquake of magnitude 5.75–6 (Rhie and Romanowicz 2004). Given the earthbound albedo of 0.306, the solar flux for Earth is eightfold that of Mars, which corresponds to magnitude 0.6 greater and therefore an extrapolation of 5.3. Nevertheless, all these estimates of magnitudes, although comparable, are less than the magnitude of 5.9 (i.e., 10^{18} Nm) which is considered by several studies as a prerequisite for detecting normal modes. Therefore, we will focus our next analysis on the possibility of coherent stacking for MBFs, which, for a Mars year of 687 days, might lead to an increase in amplitudes by $\approx 26\epsilon$, where ϵ is the fraction of daily coherent hum. For a sol-to-sol coherency exceeding 0.4, this might lead to an order of magnitude increase in signal, allowing signals to possibly peak out of the noise after stacking data over a year.

4.4 Weather Correlation and Stacking Method

The Martian surface has low thermal inertia because it is devoid of oceans. Thus, the diurnal surface-temperature cycle is very large. Combined with the very thin atmosphere, this makes thermal tides a prominent element of diurnal variability on Mars. This is further reinforced by the equatorial location of InSight. Mars has a clear dichotomy whereby low lands dominate the southern hemisphere, while the northern hemisphere is dominated by highlands. The boundary of the dichotomy is close to the equator and this dichotomy contributes

Fig. 17 Pressure correlations in normal mode frequency band. Large correlations are diurnal and semi-diurnal. On a given day, the large correlations are the sunrise-sunrise and sunset-sunset correlations. Semi-diurnal correlations are sunrise-sunset and sunset-sunrise (semi-diurnal thermal tide). The periodic excitation force generates high-efficiency stacking. This precise phenomenon occurs on Mars but not on Earth

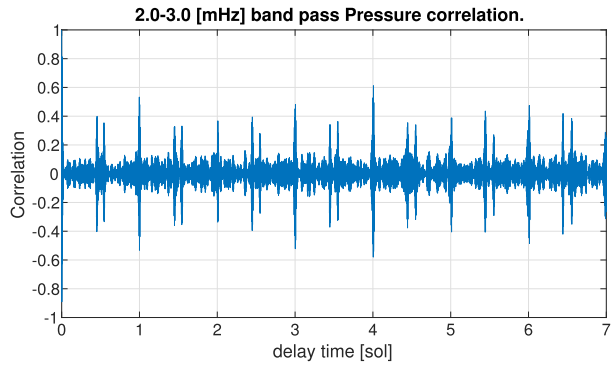
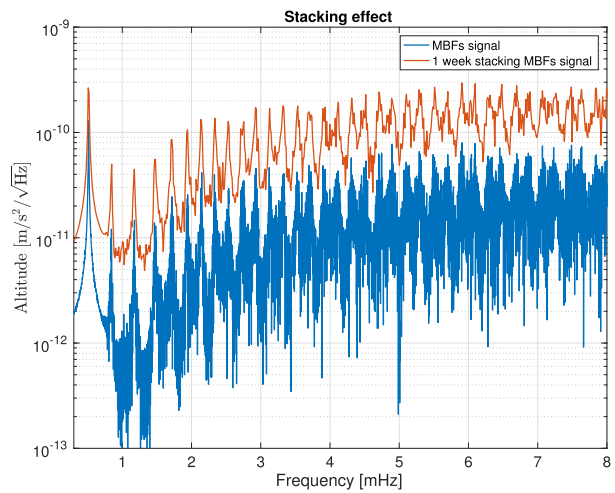


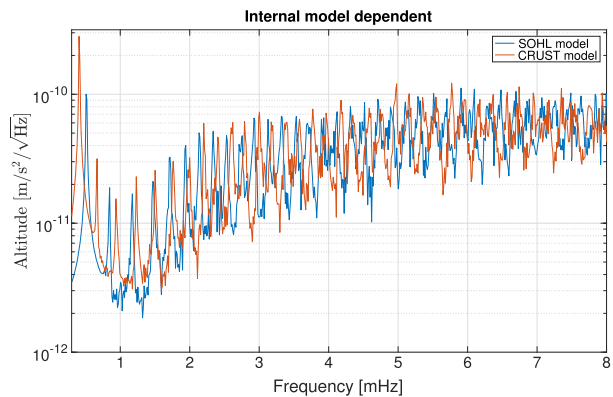
Fig. 18 Stacking efficiency for one week of data. Blue curve is MBF power density. Red line is MBF power density after one week of stacking. Daily stacking leads to large, clear peaks. The longer MBFs are stacked, the larger and sharper the normal mode peaks become. One week of stacking already leads to a significant improvement in the signal-to-noise ratio, which demonstrates that Martian stacking is far more effective than terrestrial stacking. As a result of such efficient stacking for Mars, some MBF peaks are likely to be detected by the InSight SEIS seismometer



to the diurnal cycle through slope-induced circulations, although the day-to-day variability associated with baroclinic waves is small (Spiga et al. 2018). Thus, provided we consider atmospheric variability within a given season, a significant daily repetition of atmospheric temperature, wind, and pressure should be the norm. This will correlate strongly with the diurnal range in our seismic computations derived from GCM simulations (Fig. 17), which means that stacking is likely to be an efficient way to increase the MBF amplitude above that of the self-noise or other noise sources. We tested this hypothesis with a one-week stack from the GCM simulation. The 7 sol-long data were divided into 7 time series of 24.6 hours. The results shown in Fig. 18 indicate a threefold increase in the amplitudes of stacks over 7 sols. Although extrapolation over a long period will require further GCM modeling, and because the sol-to-sol correlation might weaken over weeks, these preliminary results suggest that stacking the seismic signal over the sol time might enable significant to very significant amplification of the Mars hum. Furthermore, detecting the normal mode frequencies will allow the inversion of the Mars upper mantle, as already illustrated by Panning et al. (2017). The position of the normal mode peaks depends on the internal structure, as shown on Fig. 19. These simulations were done with two different internal structure models for Mars and the results show that the resolution after the stacking suffices to adequately shift associated with the structures.

Fig. 19

Internal-model-dependent MBFs. We use two internal models of Mars, which results in differing peak positions. The difference in peak positions corresponds to the difference in the internal structure of Mars, and the seismometer on InSight can detect this difference in frequencies. If we can detect these peaks, we can determine the internal structure of Mars



5 Conclusion

This study evaluates the magnitude of the signal of Mars' background free oscillations by using high-precision GCMs. Given the limitation of GCMs, the values obtained should be regarded as a lower limit of the possible amplitude of background free oscillations expected on Mars.

To obtain a realistic evaluation, we make several assumptions that are based on observations and theory to simplify the model and take into account the three-dimensional atmospheric structure of Mars.

Given these models and assumptions, the results indicate that MBF amplitudes are likely to be on the order of nanogals, which is consistent with previous studies, such as Kobayashi and Nishida (1998b), Lognonné and Johnson (2007). We also confirmed that the values obtained are consistent with solar flux. These results imply that the values obtained represent the typical strength of MBF signals, although the amplitudes may differ because of the assumptions used, such as those involving the internal structure and atmospheric model.

Given the level of MBF signal and the level of noise from the InSight SEIS instruments, detecting MBF signals with the InSight SEIS instruments will remain difficult. However, because the detection strategy exploits the daily repetition of the Martian atmosphere, stacking is found to be a powerful tool to overcome this problem.

The results should be viewed as a minimum estimate for MBF detection by the InSight SEIS seismometer. Knowledge of the Martian MBFs should allow us to estimate the deep internal structure of Mars and can be one of successes of the InSight mission.

Acknowledgements The authors are grateful for the support of CNES for the development of the SEIS experiment and its scientific support, and to the ANR for supporting the project through ANR SEISMARS. Y.K. acknowledges the support of the CNES and JSPC for his Ph.D. support. P.L. and A.S. acknowledge the support of IUF. This is IPGP contribution number 4010 and InSight contribution number 74.

Publisher's Note Springer Nature remains neutral with regard to jurisdictional claims in published maps and institutional affiliations.

References

- G. Backus, M. Mulcahy, Moment tensors and other phenomenological descriptions of seismic sources—I. Continuous displacements. *Geophys. J. Int.* **46**(2), 341–361 (1976)

- H. Benioff, J.C. Harrison, L. LaCoste, W.H. Munk, L.B. Slichter, Searching for the Earth's free oscillations. *J. Geophys. Res.* **64**(9), 1334–1337 (1959)
- H. Benioff, F. Press, S. Smith, Excitation of the free oscillations of the Earth by earthquakes. *J. Geophys. Res.* **66**(2), 605–619 (1961)
- B.A. Bolt, J.S. Derr, Free bodily vibrations of the terrestrial planets. *Vistas Astron.* **11**, 69–102 (1969)
- A. Colaitis, A. Spiga, F. Hourdin, C. Rio, F. Forget, E. Millour, A thermal plume model for the Martian convective boundary layer. *J. Geophys. Res., Planets* **118**(7), 1468–1487 (2013)
- F.A. Dahlen, J. Tromp, *Theoretical Global Seismology* (Princeton University Press, Princeton, 1998)
- M. Deen, E. Wielandt, E. Stutzmann, W. Crawford, G. Barruol, K. Sigloch, First observation of the Earth's permanent free oscillations on ocean bottom seismometers. *Geophys. Res. Lett.* **44**(21), 10,988–10,996 (2017). <https://doi.org/10.1002/2017GL074892>
- A.M. Dziewonski, D.L. Anderson, Preliminary reference Earth model. *Phys. Earth Planet. Inter.* **25**(4), 297–356 (1981)
- F. Forget, S. Lebonnois, Global climate models of the terrestrial planets. *Comp. Climatol. Terr. Planets* **1**, 213–229 (2013)
- F. Forget, F. Hourdin, R. Fournier, C. Hourdin, O. Talagrand, M. Collins, S.R. Lewis, P.L. Read, J-P. Huot, Improved general circulation models of the Martian atmosphere from the surface to above 80 km. *J. Geophys. Res., Planets* **104**(E10), 24155–24175 (1999)
- P. Goldreich, D.A. Keeley, Solar seismology. II. The stochastic excitation of the solar p-modes by turbulent convection. *Astrophys. J.* **212**, 243–251 (1977)
- P. Goldreich, P. Kumar, The interaction of acoustic radiation with turbulence. *Astrophys. J.* **326**(1), 462–478 (1988)
- M.P. Golombek, W.B. Banerdt, K.L. Tanaka, D.M. Tralli, A prediction of Mars seismicity from surface faulting. *Science* **258**(5084), 979–981 (1992)
- T.V. Gudkova, V.N. Zharkov, Mars: interior structure and excitation of free oscillations. *Phys. Earth Planet. Inter.* **142**(1–2), 1–22 (2004)
- B. Gutenberg, C.F. Richter, Earthquake magnitude, intensity, energy, and acceleration: (second paper). *Bull. Seismol. Soc. Am.* **46**(2), 105–145 (1956)
- R.M. Haberle, M.M. Joshi, J.R. Murphy, J.R. Barnes, J.T. Schofield, G. Wilson, M. Lopez-Valverde, J.L. Hollingsworth, A.F.C. Bridger, J. Schaeffer, General circulation model simulations of the Mars Pathfinder atmospheric structure investigation/meteorology data (1999)
- P. Julián, M. Jordán, A. Desages, Canonical piecewise-linear approximation of smooth functions. *IEEE Trans. Circuits Syst. I, Fundam. Theory Appl.* **45**(5), 567–571 (1998)
- V.G. Kaydash, M.A. Kreslavsky, Y.G. Shkuratov, G. Videen, J.F. Bell III, M. Wolff, Measurements of winds on Mars with Hubble Space Telescope images in 2003 opposition. *Icarus* **185**(1), 97–101 (2006)
- B. Kenda, P. Lognonné, A. Spiga, T. Kawamura, S. Kedar, W.B. Banerdt, R. Lorenz, D. Banfield, M. Golombek, Modeling of ground deformation and shallow surface waves generated by Martian dust devils and perspectives for near-surface structure inversion. *Space Sci. Rev.* **211**(1–4), 501–524 (2017)
- A. Khan, J.A.D. Connolly, Constraining the composition and thermal state of Mars from inversion of geophysical data. *LPI Contributions*, No. 1353 (2007), p. 3013
- M. Knapmeyer, J. Oberst, E. Hauber, M. Wählisch, C. Deuchler, R. Wagner, Working models for spatial distribution and level of Mars' seismicity. *J. Geophys. Res., Planets* **111**(E11) (2006)
- N. Kobayashi, K. Nishida, Atmospheric excitation of planetary free oscillations. *J. Phys. Condens. Matter* **10**(49), 11557 (1998a)
- N. Kobayashi, K. Nishida, Continuous excitation of planetary free oscillations by atmospheric disturbances. *Nature* **395**(6700), 357–360 (1998b)
- R.L. Kovach, D.L. Anderson, The interiors of the terrestrial planets. *J. Geophys. Res.* **70**(12), 2873–2882 (1965)
- G. Laske, R. Widmer-Schmidrig, *Treatise on Geophysics, Theory and Observations: Normal Mode and Surface Wave Observations*, vol. 1.04 (Elsevier, Amsterdam, 2015)
- P. Lognonné, Normal modes and seismograms in an anelastic rotating Earth. *J. Geophys. Res., Solid Earth* **96**(B12), 20309–20319 (1991)
- P. Lognonné, Normal modes of the Earth and planets, in *Handbook on Earthquake and Engineering Seismology* (2002), pp. 125–147
- P. Lognonné, Planetary seismology. *Annu. Rev. Earth Planet. Sci.* **33**, 571–604 (2005)
- P. Lognonné, D. Giardini, The NetLander very broad band seismometer. *Planet. Space Sci.* **48**, 1289–1302 (2000)
- P. Lognonné, C.L. Johnson, *Planetary Seismology*, vol. 10.03 (Elsevier, Amsterdam, 2007)
- P. Lognonné, C.L. Johnson, *Planetary Seismology*, vol. 10.03 (Elsevier, Amsterdam, 2015)
- P. Lognonné, B. Mosser, Planetary seismology. *Surv. Geophys.* **14**(3), 239–302 (1993)

- P. Lognonné, B. Mosser, F.A. Dahlen, Excitation of jovian seismic waves by the Shoemaker-Levy 9 cometary impact. *Icarus* **110**(2), 180–195 (1994)
- P. Lognonné, J.G. Beyneix, W.B. Banerdt, S. Cacho, J.F. Karczewski, M. Morand, Ultra broad band seismology on InterMarsNet. *Planet. Space Sci.* **44**(11), 1237–1249 (1996)
- P. Lognonné, E. Clévéde, H. Kanamori, Computation of seismograms and atmospheric oscillations by normal-mode summation for a spherical Earth model with realistic atmosphere. *Geophys. J. Int.* **135**(2), 388–406 (1998a)
- P. Lognonné, V.N. Zharkov, J.F. Karczewski, B. Romanowicz, M. Menvielle, G. Poupinet, B. Brient, C. Cavoit, A. Desautz, B. Dole et al., The seismic optimism experiment. *Planet. Space Sci.* **46**(6–7), 739–747 (1998b)
- P. Lognonné, T. Spohn, D. Mimoun, S. Ulamec, J. Biele, GEP-ExoMars: a geophysics and environment observatory on Mars, in *37th Annual Lunar and Planetary Science Conference*, vol. 37 (2006)
- P. Lognonné, W.T. Pike, V. Tong, R. Garcia, Planetary seismometry, in *Extraterrestrial Seismology* (2015), pp. 36–48
- P. Lognonné, F. Karakostas, L. Rolland, Y. Nishikawa, Modeling of atmospheric-coupled Rayleigh waves on planets with atmosphere: from Earth observation to Mars and Venus perspectives. *J. Acoust. Soc. Am.* **140**(2), 1447–1468 (2016)
- P. Lognonné, W.B. Banerdt, D. Giardini, W.T. Pike, U. Christensen, P. Laudet, S. de Raucourt, P. Zweifel, S. Calcutt, M. Bierwirth, K.J. Hurst, F. Ijpelaan, J.W. Umland, R. Llorca-Cejudo, S.A. Larson, R.F. Garcia, S. Kedar, B. Knapmeyer-Endrun, D. Mimoun, A. Mocquet, M.P. Panning, R.C. Weber, A. Sylvestre-Baron, G. Pont, N. Verdier, L. Kerjean, L.J. Facto, V. Gharakanian, J.E. Feldman, T.L. Hoffman, D.B. Klein, K. Klein, N.P. Onufer, J. Paredes-Garcia, M.P. Petkov, J.R. Willis, S.E. Smrekar, M. Drilleau, T. Gabsi, T. Nebut, O. Robert, S. Tillier, C. Moreau, M. Parise, G. Aveni, S. Ben Charef, Y. Bennour, T. Camus, P.A. Dandonneau, C. Desfoux, B. Lecomete, O. Pot, P. Revuz, D. Mance, J. tenPierick, N.E. Bowles, C. Charalambous, A.K. Delahunty, J. Hurley, R. Irshad, H. Liu, A.G. Mukherjee, I.M. Standley, A.E. Stott, J. Temple, T. Warren, M. Eberhardt, A. Kramer, W. Kühne, E.-P. Miettinen, M. Monecke, C. Aicardi, M. André, J. Baroukh, A. Borrien, A. Bouisset, P. Boutte, K. Brethomé, C. Brysbaert, T. Carlier, M. Deleuze, J.M. Desmarres, D. Dilhan, C. Doucet, D. Faye, N. Faye-Refalo, R. Gonzalez, C. Imbert, C. Larigauderie, E. Locatelli, L. Luno, J.-R. Meyer, F. Mialhe, J.M. Mouret, M. Nonon, Y. Pahn, A. Paillet, P. Pasquier, G. Perez, R. Perez, L. Perrin, B. Pouilloux, A. Rosak, I. Savin de Larclause, J. Sicre, M. Sodki, N. Toulemon, B. Vella, C. Yana, F. Alibay, O.M. Avalos, M.A. Balzer, P. Bhandari, E. Blanco, B.D. Bone, J.C. Bousman, P. Bruneau, F.J. Calef, R.J. Calvet, S.A. D'Agostino, G. de los Santos, R.G. Deen, R.W. Denise, J. Ervin, N.W. Ferraro, H.E. Gengf, F. Grinblat, D. Hernandez, M. Hetzel, M.E. Johnson, L. Khachikyan, J.Y. Lin, S.M. Madzunkov, S.L. Marshall, I.G. Mikellides, E.A. Miller, W. Raff, J.E. Singer, C.M. Sunday, J.F. Villalvazo, M.C. Wallace, D. Banfield, J.A. Rodriguez-Manfredi, C.T. Russell, A. Trebi-Ollennu, J.N. Maki, E. Beucler, M. Böse, C. Bonjour, J.L. Berenguer, S. Ceylan, J. Clinton, V. Conejero, I. Daubar, V. Dehant, P. Delage, F. Euchner, I. Estève, L. Fayon, L. Ferraioli, C.L. Johnson, J. Gagnepain-Beyneix, M. Golombek, A. Khan, T. Kawamura, B. Kenda, P. Labrot, N. Murdoch, C. Pardo, C. Perrin, L. Pou, A. Sauron, D. Savoie, S. Stähler, E. Stutzmann, N.A. Teanby, J. Tromp, M. van Driel, M. Wiczorek, R. Widmer-Schnidrig, J. Wookey, SEIS: Insight's Seismic Experiment for Internal Structure of Mars. *Space Sci. Rev.* **215**(1), 12 (2019). <https://doi.org/10.1007/s11214-018-0574-6>
- J-B. Madeleine, F. Forget, E. Millour, L. Montabone, M.J. Wolff, Revisiting the radiative impact of dust on Mars using the LMD global climate model. *J. Geophys. Res., Planets* **116**(E11) (2011)
- G.M. Martínez, C.N. Newman, A. De Vicente-Retortillo, E. Fischer, N.O. Renno, M.I. Richardson, A.G. Fairén, M. Genzer, S.D. Guzewich, R.M. Haberle, A.-M. Harri, O. Kempainen, M.T. Lemmon, M.D. Smith, M. de la Torre-Juárez, A.R. Vasavada, The modern near-surface Martian climate: a review of in-situ meteorological data from viking to curiosity. *Space Sci. Rev.* **212**(1), 295–338 (2017). <https://doi.org/10.1007/s11214-017-0360-x>
- R. Millot-Langet, E. Clévéde, P. Lognonné, Realistic long period synthetic seismograms using normal modes of a 3d anelastic elliptic rotating Earth, in *EGS General Assembly Conference Abstracts*, vol. 27 (2002)
- D. Mimoun, N. Murdoch, P. Lognonné, T. Pike, K. Hurst et al. (SEIS Team), The seismic noise model of the InSight mission to Mars. *Space Sci. Rev.* (2016)
- L. Montabone, F. Forget, E. Millour, R.J. Wilson, S.R. Lewis, B. Cantor, D. Kass, A. Kleinböhl, M.T. Lemmon, M.D. Smith et al., Eight-year climatology of dust optical depth on Mars. *Icarus* **251**, 65–95 (2015)
- J.P. Montagner, *Treatise on Geophysics, Deep Earth Structure: Upper Mantle Structure: Global Isotropic and Anisotropic Elastic Tomography*, vol. 1.19 (Elsevier, Amsterdam, 2015)
- N. Murdoch, B. Kenda, T. Kawamura, A. Spiga, P. Lognonné, D. Mimoun, W.B. Banerdt, Estimations of the seismic pressure noise on Mars determined from Large Eddy Simulations and demonstration of pressure decorrelation techniques for the InSight mission. *Space Sci. Rev.* **211**(1–4), 457–483 (2017)

- J.R. Murphy, C.B. Leovy, J.E. Tillman, Observations of Martian surface winds at the Viking Lander 1 site. *J. Geophys. Res., Solid Earth* (1978–2012) **95**(B9), 14555–14576 (1990)
- T. Navarro, J.-B. Madeleine, F. Forget, A. Spiga, E. Millour, F. Montmessin, A. Määttänen, Global climate modeling of the Martian water cycle with improved microphysics and radiatively active water ice clouds. *J. Geophys. Res., Planets* **119**(7), 1479–1495 (2014)
- K. Nishida, Earth's background free oscillations. *Annu. Rev. Earth Planet. Sci.* **41**, 719–740 (2013a)
- K. Nishida, Global propagation of body waves revealed by cross-correlation analysis of seismic hum. *Geophys. Res. Lett.* **40**(9), 1691–1696 (2013b)
- K. Nishida, Source spectra of seismic hum. *Geophys. J. Int.* **199**(1), 416–429 (2014)
- K. Nishida, Ambient seismic wave field. *Proc. Jpn. Acad. Ser. B* **93**(7), 423–448 (2017)
- K. Nishida, N. Kobayashi, Y. Fukao, Resonant oscillations between the solid earth and the atmosphere. *Science* **287**(5461), 2244–2246 (2000)
- K. Nishida, J.-P. Montagner, H. Kawakatsu, Global surface wave tomography using seismic hum. *Science* **326**(5949), 112 (2009)
- E.A. Okal, D.L. Anderson, Theoretical models for Mars and their seismic properties. *Icarus* **33**(3), 514–528 (1978)
- M.P. Panning, P. Lognonné, W.B. Banerdt, R. García, M. Golombek, S. Kedar, B. Knapmeyer-Endrun, A. Mocquet, N.A. Teanby, J. Tromp et al., Planned products of the Mars structure service for the InSight mission to Mars. *Space Sci. Rev.* **211**(1–4), 611–650 (2017)
- A. Petrosyan, B. Galperin, S.E. Larsen, S.R. Lewis, A. Määttänen, P.L. Read, N. Renno, L.P.H.T. Rogberg, H. Savijärvi, T. Siili et al., The Martian atmospheric boundary layer. *Rev. Geophys.* **49**(3) (2011)
- R.J. Phillips, R.E. Grimm, Martian seismicity, in *Lunar and Planetary Science Conference*, vol. 22 (1991), pp. 1061–1062
- A. Pottier, F. Forget, F. Montmessin, T. Navarro, A. Spiga, E. Millour, A. Szantai, J.-B. Madeleine, Unraveling the Martian water cycle with high-resolution global climate simulations. *Icarus* (2017). <https://doi.org/10.1016/j.icarus.2017.02.016>
- P.L. Read, S.R. Lewis, *The Martian Climate Revisited: Atmosphere and Environment of a Desert Planet* (Springer, Berlin, 2004)
- J. Rhie, B. Romanowicz, Excitation of Earth's continuous free oscillations by atmosphere–ocean–seafloor coupling. *Nature* **431**(7008), 552 (2004)
- J. Rhie, B. Romanowicz, A study of the relation between ocean storms and the Earth's hum. *Geochem. Geophys. Geosyst.* **7**(10) (2006)
- A. Rivoldini, T. Van Hoolst, O. Verhoeven, A. Mocquet, V. Dehant, Geodesy constraints on the interior structure and composition of Mars. *Icarus* **213**(2), 451–472 (2011)
- B.A. Romanowicz, B.J. Mitchell, *Treatise on Geophysics, Deep Earth Structure: Q of the Earth from Crust to Core*, vol. 1.19 (Elsevier, Amsterdam, 2015)
- M. Schimmel, E. Stutzmann, J. Gallart, Using instantaneous phase coherence for signal extraction from ambient noise data at a local to a global scale. *Geophys. J. Int.* **184**(1), 494–506 (2011). <https://doi.org/10.1111/j.1365-246X.2010.04861.x>
- M. Schimmel, E. Stutzmann, S. Ventosa, Low-frequency ambient noise autocorrelations: waveforms and normal modes. *Seismol. Res. Lett.* **89**(4), 1488–1496 (2018). <https://doi.org/10.1785/0220180027>
- J.T. Schofield, J.R. Barnes, D. Crisp, R.M. Haberle, S. Larsen, J.A. Magalhaes, J.R. Murphy, A. Seiff, G. Wilson, The Mars Pathfinder atmospheric structure investigation/meteorology (ASI/MET) experiment. *Science* **278**(5344), 1752–1758 (1997)
- S.E. Smrekar, P. Lognonné, T. Spohn, W.B. Banerdt, D. Breuer, U. Christensen, V. Dehant, M. Drilleau, W. Folkner, N. Fuji, R.F. Garcia, D. Giardini, M. Golombek, M. Grott, T. Gudkova, C. Johnson, A. Khan, B. Langlais, A. Mittelholz, A. Mocquet, R. Myhill, M. Panning, C. Perrin, T. Pike, A.-C. Plesa, A. Rivoldini, H. Samuel, S.C. Stähler, M. van Driel, T. Van Hoolst, O. Verhoeven, R. Weber, M. Wieczorek, Pre-mission InSights on the Interior of Mars. *Space Sci. Rev.* **215**(1), 3 (2018). <https://doi.org/10.1007/s11214-018-0563-9>
- F. Sohl, T. Spohn, The interior structure of Mars: implications from SNC meteorites. *J. Geophys. Res., Planets* **102**, 1613–1635 (1997)
- S.C. Solomon, D.L. Anderson, W.B. Banerdt, R.G. Butler, P.M. Davis, F.K. Duennebier, Y. Nakamura, E.A. Okal, R.J. Phillips, Scientific rationale and requirements for a global seismic network on Mars (1991)
- A. Spiga, Elements of comparison between Martian and terrestrial mesoscale meteorological phenomena: katabatic winds and boundary layer convection. *Planet. Space Sci.* **59**(10), 915–922 (2011)
- A. Spiga, F. Forget, A new model to simulate the Martian mesoscale and microscale atmospheric circulation: validation and first results. *J. Geophys. Res., Planets* **114**(E2) (2009)
- A. Spiga, S.R. Lewis, Martian mesoscale and microscale wind variability of relevance for dust lifting. *Mars* **5**, 146–158 (2010)

- A. Spiga, D. Banfield, N.A. Teanby, F. Forget, A. Lucas, B. Kenda, J.A. Rodriguez Manfredi, R. Widmer-Schmidrig, N. Murdoch, M.T. Lemmon, R.F. Garcia, L. Martire, Ö. Karatekin, S. Le Maistre, B. Van Hove, V. Dehant, P. Lognonné, N. Mueller, R. Lorenz, D. Mimoun, S. Rodriguez, É. Beucler, I. Daubar, M.P. Golombek, T. Bertrand, Y. Nishikawa, E. Millour, L. Rolland, Q. Brissaud, T. Kawamura, A. Mocquet, R. Martin, J. Clinton, É. Stutzmann, T. Spohn, S. Smrekar, W.B. Banerdt, Atmospheric science with InSight. *Space Sci. Rev.* **214**, 109 (2018). <https://doi.org/10.1007/s11214-018-0543-0>
- T. Spohn, M.H. Acuña, D. Breuer, Geophysical constraints on the evolution of Mars. *Space Sci. Rev.* **96**, 231–262 (2001)
- N. Suda, K. Nawa, Y. Fukao, Earth's background free oscillations. *Science* **279**(5359), 2089–2091 (1998)
- T. Tanimoto, Continuous free oscillations: atmosphere-solid earth coupling. *Annu. Rev. Earth Planet. Sci.* **29**(1), 563–584 (2001)
- T. Tanimoto, The oceanic excitation hypothesis for the continuous oscillations of the Earth. *Geophys. J. Int.* **160**(1), 276–288 (2005)
- T. Tanimoto, J. Um, Cause of continuous oscillations of the Earth. *J. Geophys. Res., Solid Earth* **104**(B12), 28723–28739 (1999)
- V.C.H. Tong, R.A. García, *Extraterrestrial Seismology* (Cambridge University Press, Cambridge, 2015)
- T. Van Hoolst, V. Dehant, F. Roosbeek, P. Lognonné, Tidally induced surface displacements, external potential variations, and gravity variations on Mars. *Icarus* **161**(2), 281–296 (2003)
- S. Ventosa, M. Schimmel, E. Stutzmann, Extracting surface waves, hum and normal modes: time-scale phase-weighted stack and beyond. *Geophys. J. Int.* **211**(1), 30–44 (2017). <https://doi.org/10.1002/2017JB014354>
- S. Watada, H. Kanamori, Acoustic resonant oscillations between the atmosphere and the solid earth during the 1991 Mt. Pinatubo eruption. *J. Geophys. Res. Solid Earth* **115**(B12) (2010)
- S. Watada, G. Masters, Oceanic excitation of the continuous oscillations of the Earth, in *AGU Fall Meeting Abstracts* (2001), art. S32A-0620
- S.C. Webb, The Earth's hum is driven by ocean waves over the continental shelves. *Nature* **445**(7129), 754 (2007)
- J.H. Woodhouse, A. Deuss, *Theory and Observations – Earth's Free Oscillations*, vol. 1.03 (Elsevier, Amsterdam, 2015)
- V.N. Zharkov, T.V. Gudkova, On the dissipative factor of the Martian interiors. *Planet. Space Sci.* **45**(4), 401–407 (1997)